

Opto-Electronic Advances

CN 51-1781/TN ISSN 2096-4579 (Print) ISSN 2097-3993 (Online)

Tunable vertical cavity microlasers based on MAPbI₃ phase change perovskite

Rongzi Wang, Ying Su, Hongji Fan, Chengxiang Qi, Shuang Zhang and Tun Cao

Citation: Wang RZ, Su Y, Fan HJ, et al. Tunable vertical cavity microlasers based on MAPbI₃ phase change perovskite. *Opto-Electron Adv* 8, 240220(2025).

<https://doi.org/10.29026/oea.2025.240220>

Received: 18 September 2024; Accepted: 20 January 2025; Published online: 28 March 2025

Related articles

Non-volatile dynamically switchable color display via chalcogenide stepwise cavity resonators

Kuan Liu, Zhenyuan Lin, Bing Han, Minghui Hong, Tun Cao

Opto-Electronic Advances 2024 7, 230033 doi: [10.29026/oea.2024.230033](https://doi.org/10.29026/oea.2024.230033)

More related article in Opto-Electronic Journals Group website 



<http://www.oejournal.org/oea>



 OE_Journal



 @OptoElectronAdv

DOI: [10.29026/oea.2025.240220](https://doi.org/10.29026/oea.2025.240220)CSTR: [32247.14.oea.2025.240220](https://cstr.net/urn:CSTR:32247.14.oea.2025.240220)

Tunable vertical cavity microlasers based on MAPbI₃ phase change perovskite

Rongzi Wang^{1†}, Ying Su^{1†}, Hongji Fan¹, Chengxiang Qi¹,
Shuang Zhang^{2,3,4} and Tun Cao^{1†*}

Perovskite semiconductors show great promise as gain media for all-solution-processed single-mode microlasers. However, despite the recent efforts to improve their lasing performance, achieving tunable single-mode microlasers remains challenging. In this work, we address this challenge by demonstrating a tunable vertical cavity surface emitting laser (VCSEL) employing a tunable gain medium of halide phase-change perovskites—specifically MAPbI₃ perovskite, sandwiched between two highly reflective mirrors composed of bottom-distributed Bragg reflectors (DBRs). This VCSEL possesses single-mode lasing emission with a low threshold of 23.5 μJ cm⁻² under 160 K, attributed to strong optical confinement in the high-quality (Q) cavity. Upon the phase change of MAPbI₃ perovskite, both its gain and dielectric constant changes dramatically, enabling a wide ($\Delta\lambda > 9$ nm) and temperature-sensitive (0.30 nm K⁻¹ rate) spectral tunability of lasing mode in the near-infrared (N-IR) region. The laser displays excellent stability, demonstrating an 80% lifetime of $> 2.4 \times 10^7$ pulses excitation. Our findings may provide a versatile platform for the next generation of tunable coherent light sources.

Keywords: tunable; perovskite; phase change; vertical cavity surface emitting laser

Wang RZ, Su Y, Fan HJ et al. Tunable vertical cavity microlasers based on MAPbI₃ phase change perovskite. *Opto-Electron Adv* **8**, 240220 (2025).

Introduction

Solution-processed halide perovskite semiconductors are emerging as a promising photonic material platform with potential applications in various fields, including lasers¹⁻³, light-emitting diodes⁴⁻⁶, and solar cells⁷⁻⁹. Halide perovskite has been considered as an exceptional gain material for low-cost lasers due to its high photoluminescence quantum yield, bandgap tunability, and narrow radiation spectrum¹⁰⁻¹². Since Deschler et al. demonstrated an optically pumped lasing from halide perovskite in 2014¹³, perovskite lasers have been construct-

ed using different kinds of external microcavities, such as Fabry-Pérot (F-P) cavities¹⁴, photonic crystal (PC)^{15,16}, and whispering-gallery-mode (WGM)¹⁷⁻¹⁹. Distributed feedback (DFB) and vertical cavity surface emitting perovskite lasers have been recently investigated, enabling greater control of the wavelength and beam shape of the laser²⁰⁻²³. However, they have been constrained to operate at a fixed wavelength.

In the digital field, where the lasers are widely used in integrated forms, tunable and compact lasers are highly desired. Recently, tunable compact photonics devices

¹School of Optoelectronic Engineering and Instrumentation Science, Dalian University of Technology, Dalian 116024, China; ²New Cornerstone Science Laboratory, Department of Physics, University of Hong Kong, Hong Kong 999077, China; ³Department of Electrical & Electronic Engineering, University of Hong Kong, Hong Kong 999077, China; ⁴Materials Innovation Institute for Life Sciences and Energy (MILES), HKU-SIRI, Shenzhen 518052, China.

[†]These authors contributed equally to this work.

*Correspondence: T Cao, E-mail: caotun1806@dlut.edu.cn

Received: 18 September 2024; Accepted: 20 January 2025; Published online: 28 March 2025



Open Access This article is licensed under a Creative Commons Attribution 4.0 International License.

To view a copy of this license, visit <http://creativecommons.org/licenses/by/4.0/>.

© The Author(s) 2025. Published by Institute of Optics and Electronics, Chinese Academy of Sciences.

based on phase change materials (PCMs), such as chalcogenide glass^{24–28} and vanadium dioxide^{29,30}, have attracted much attention³¹. Nevertheless, although the PCMs have been broadly exploited in the transmissive and reflective structures, they cannot be used for realizing tunable lasers due to the absence of optical gain. Therefore, developing the PCM possessing tunable dielectric constant and optical gain is necessary, which can provide solutions for tunable light-emitting devices.

Halide perovskites are a burgeoning family of photonics materials, benefitting from their high permittivity and extraordinary luminescence performance³². They have been applied to dielectric nanophotonic structures³³ and light-radiating devices^{34,35} such as photoluminescence-enhanced metamaterials^{36,37}, high-resolution color displays^{38–40}, and low-threshold lasers^{41–43}. Moreover, due to the strong interference between organic ligands and inorganic framework, halide perovskites exhibit a rich variety of crystallographic states that can be controlled by pressure⁴⁴, chemical composition⁴⁵, and temperature⁴⁶. These state transitions can induce significant variation in refractive index⁴⁷. Notably, the excitons in the halide perovskites possess a small Bohr radius and efficient electrostatic Coulomb coupling, resulting in their distinct optical characteristics, including effective quantum yield, great exciton binding energy, and efficient radiative recombination⁴⁸. Because of these excellent features, halide perovskites are promising candidates for the gain medium in the lasing applications⁴⁹. Nevertheless, the usages of halide perovskites as a phase-change tunable gain medium have yet to be exploited.

Here, we present a spectrally tunable single-mode vertical-cavity near-infrared (NIR) microlaser, based on MAPbI₃ halide perovskite film, which acts as a phase-change tunable gain medium. The high-quality (*Q*) factor vertical cavity consists of two highly reflectors (Au mirror and distributed Bragg reflector (DBR)) parallel to each other, with the methylammonium lead iodide CH₃NH₃PbI₃ (MAPbI₃) gain medium sandwiched between them. The change in luminescence and refractive index upon structural state change leads to a broad spectral tunability in lasing frequency ranging from 790.6 nm to 799.7 nm, and with a significant tuning rate of ~0.30 nm K⁻¹. This rate is one order higher in magnitude compared to the traditional semiconductor lasers⁵⁰. The single-mode lasing emission with excellent spatial coherence can be readily obtained through this simple vertical-cavity. The constructed vertical cavity surface emitting

laser (VCSEL) exhibits extraordinary performance, with a low lasing threshold of ~23.5 μJ cm⁻², and a broad tuning range of the emission frequency from 790.6 nm to 799.7 nm. In addition, the device maintains its performance over 2.4×10⁷ cycles of optical pulse excitation with a duration of ~50 min. Our work not only advances the development of tunable perovskite VCSELs but also shed light on the next generation of the integrated photonics.

Results and discussion

For the demonstration of the phase-change perovskite tunable VCSEL, we have chosen a prototypical halide perovskite, MAPbI₃, a high refractive index PCM that undergoes a phase change between tetragonal and orthorhombic at 130–160 K^{47,51} (Fig. 1(b)). This phase change leads to a substantial modulation of both refractive index and gain spectrum. The complex refractive index N_{eff} ($N_{\text{eff}} = n_{\text{eff}} + i \times k_{\text{eff}}$) of a MAPbI₃ layer in both orthorhombic and tetragonal phases is measured in the 700 nm to 850 nm spectral range using a variable angle spectroscopic ellipsometry (VASE). As shown in supplementary Fig. S1, the material possesses relatively high n_{eff} for both tetragonal and orthorhombic structural states across a wide temperature range, allowing efficient confinement and modulation of light at the subwavelength scale. The phase change can produce a remarkable tunability of the n_{eff} . The n_{eff} for the tetragonal state is much larger than the orthorhombic state over the visible-NIR spectrum from 700 nm to 850 nm, with Δn_{eff} reaching 0.19 between tetragonal phase (160 K) and orthorhombic phase (130 K) around the wavelength of 784 nm. We schematically present the structure of MAPbI₃ VCSEL fabricated on top of a quartz glass substrate in Fig. 1(a). The red square encircled by the dashed lines represents the MAPbI₃ gain film between the bottom DBR mirror and the top Au reflector. The bottom DBR reflector consists of 12 pairs of SiO₂/Ta₂O₅ stacked layers with quarter wavelength thicknesses to achieve high reflectivity. After sputtering the bottom DBR on the quartz glass substrate, we directly spin-coat MAPbI₃ on the surface of the DBR and anneal it to form the thin film. Subsequently, the Au mirror was deposited on the MAPbI₃ as the back reflector. Note that, the silver could also serve as a promising reflector due to its additional pumping efficiency. The period of the DBR and the thickness of each layer are optimized to enhance optical confinement and improve the spectral characteristics crucial to the overall device performance at the targeted lasing wavelength of

795 nm. The cross-sectional scanning electron microscope (SEM) picture of the fabricated microcavity structure is shown in Fig. 1(c), where the DBR multilayers can be clearly distinguished. Fig. 1(d) presents the SEM image (at 20000 \times magnification) of the MAPbI₃ film grown on the distributed Bragg reflector (DBR). The image clearly reveals the nanocrystal (NC) features in the synthesized MAPbI₃ perovskite, with the grain size measured in the range of several hundred nanometers. Meanwhile, we performed a statistical analysis of the crystal sizes in MAPbI₃ films based on SEM images. The detailed statistical data are presented in supplementary Fig. S2. Approximately 72% of the particle size distribution falls within the range of 100 nm to 200 nm. The surface roughnesses of the DBR mirror, the MAPbI₃ film, and the microcavity are measured using an atomic force microscope (AFM) as shown in supplementary Fig. S3. The root-mean-square (RMS) values of the surface roughness were 1.2 nm, 4.1 nm, and 11.5 nm, respectively, illustrating the high quality and smooth surface of the

microcavity VCSEL. In supplementary Fig. S4(a–c), the microscopic morphology of the MAPbI₃ film on the quartz glass substrate was measured, manifesting the outstanding crystallinity of the nanocrystalline layer. In supplementary Fig. S4(d), the temperature-dependent XRD spectra of the MAPbI₃ film were investigated, uncovering its phase transition from tetragonal to orthorhombic with decreasing temperature.

In Fig. 2(a), we show the measured absorptance and photoluminescence (PL) spectra of the MAPbI₃ thin film for both tetragonal (orange line) and orthorhombic (green line) states, respectively. The absorption edge of the tetragonal state appears around 740 nm, and the PL exhibits two peaks at around 740 nm and 787 nm. On the other hand, the absorption edge and PL peak for the orthorhombic state center occur around 780 nm and 790 nm. The PL spectra demonstrate sharp profiles with full width at half-maximum (FWHM) of \sim 25.5 nm and 24.5 nm for both tetragonal and orthorhombic states, respectively. The temperature dependence of the spontaneous

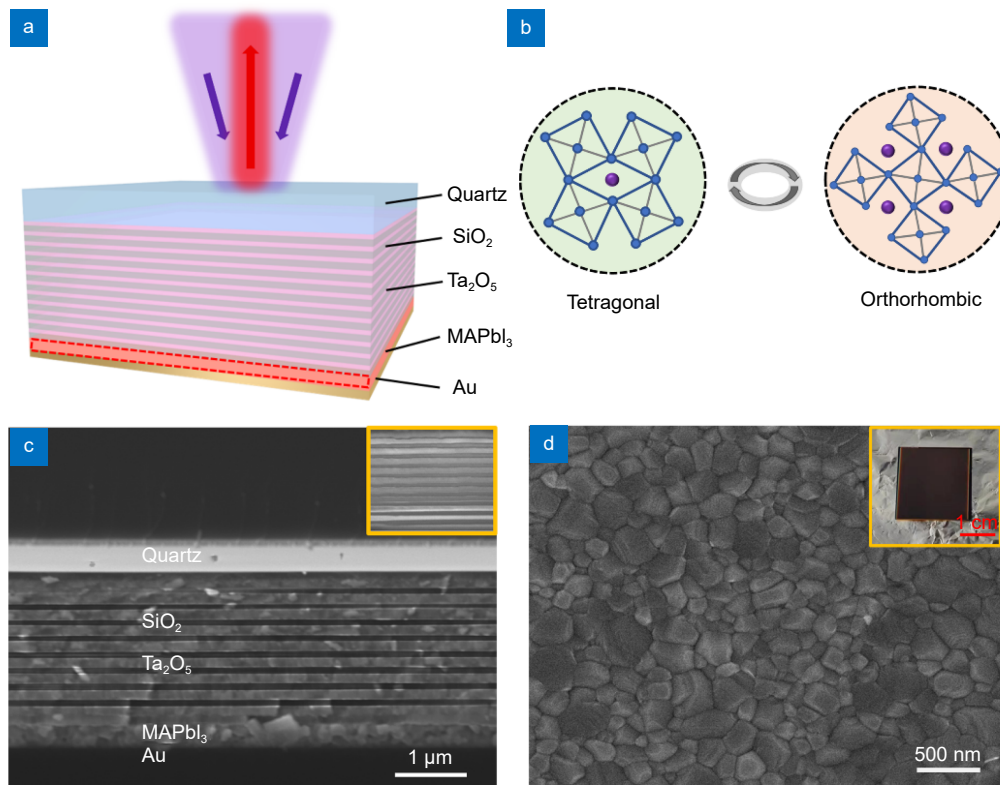


Fig. 1 | Phase-change perovskite vertical microcavity laser. (a) Schematic of a tunable microlaser based on phase-change perovskite gain medium, sandwiched between Au mirror and DBR reflector sitting on a quartz glass substrate, pumped by blue-violet laser ($\lambda = 405$ nm) and emitting a tunable beam in the near-IR from 790.7 nm to 799.5 nm. (b) Conceptual depiction of the two crystal structures of MAPbI₃, the low-temperature (130 K) orthorhombic state and room-temperature (298 K) tetragonal state. (c) Cross-sectional SEM picture of the VCSEL. The inset shows a zoomed-in image to present the optimized morphology of Ta₂O₅/SiO₂ films. Scale bar: 1 μ m. (d) The SEM image of a \sim 300 nm-thick MAPbI₃ film residing on the DBR reflectors. Scale bar: 500 nm. The inset is a photograph of the vertical microcavity, scale bar: 1 cm.

PL radiation of MAPbI₃ are characterized and shown in Fig. S5(a) and S5(b). At the tetragonal state, the PL peak center corresponding to the near-band-edge transition gradually shifts from 770 nm to 790 nm by decreasing the temperature from 298 K to 160 K. By further reducing the temperature through the tetragonal-orthorhombic phase transition, the PL begins to blueshift, and the second peak PL occurs at a shorter wavelength of 743 nm at the orthorhombic state (140 K). The quantum efficiency of the MAPbI₃ thin film was measured using a Steady-State and Transient Fluorescence and Phosphorescence Spectrometer (Edinburgh, FLS 1000), with an absolute quantum efficiency of 42% at room temperature. To investigate the suitability of MAPbI₃ as a gain medium for laser, we measure the amplified spontaneous emission (ASE) spectra of the ~300 nm thick MAPbI₃ film layer with both tetragonal (orange line) and orthorhombic (green line) states, via strip excitation^{52,53} (Fig. 2(b)). For the tetragonal MAPbI₃ layer, when the pump fluence is increased above 7.9 μJ cm⁻², distinct signatures of ASE with an ultranarrow emission linewidth of ~7 nm and a steep increase of ASE peak intensity can be observed. By changing the state of MAPbI₃ from tetragonal to orthorhombic, the emission band narrows to ~6.5 nm at the pump fluence of 4 μJ cm⁻², implying that the ASE threshold can be maintained during the phase transition. A red shift of ~12 nm for the ASE peak was also observed as the temperature increased from 130 K (tetragonal phase) to 160 K (orthorhombic phase) due to the variation in N_{eff} of MAPbI₃. The small threshold and wide tunability in ASE spectra across the phase change indicate that MAPbI₃ phase change perovskite is a promising gain dielectric for tunable lasing. To match up the peak wavelengths of ASE of MAPbI₃ film with the PL of tetragonal ($\lambda_t = 785$ nm) and orthorhombic ($\lambda_o = 805$ nm) states, both the DBR and Au mirrors should be designed to have a broad reflectance band covering the near-infrared-wavelength region. Additionally, they should remain transparent at the pumping wavelength ($\lambda_p = 405$ nm). As shown in Fig. 2(c), the normalized reflectance spectra (from 770 nm to 820 nm) of the bottom DBRs and top Au reflectors exhibit a large reflectance up to ~99.8%, while maintaining a high transparency for the wavelength less than 410 nm ($R \leq 20\%$). Such a broad high-reflectance band covers the whole ASE of the MAPbI₃ nanocrystals perovskite for both tetragonal and orthorhombic states and benefits the intense optical confinement. In Fig. 2(d), we show the

measured PL spectra of phase-change perovskite VCSEL structure in both tetragonal and orthorhombic states pumped by the low-excitation powers of 29.5 μJ cm⁻² and 8.1 μJ cm⁻², respectively. Herein, the pumping source is a femtosecond (fs) laser (1030 nm, PHAROS PH2) with optical parametric amplifier output of 130 fs pulse width, 405 nm wavelength, and 400 kHz repetition. The PL bands can be redshifted by changing the phase from tetragonal and orthorhombic by increasing the temperature from 130 K to 160 K. The uncoupled exciton spectrum is absent, showing that the photonic modes are efficiently coupled with the perovskite excitons in the vertical cavity⁵⁴.

For the VCSEL structure, the resonant mode from the vertical cavity determines the laser emission wavelength. In order to align the resonance modes of the different structural states of tetragonal and orthorhombic to their ASE spectral spectrum, we determined the thickness of the perovskite film, which is ~300 nm, as shown in supplementary Fig. S6(a). For the tetragonal (orthorhombic) state, the lasing peak occurs at $\lambda = 790.6$ nm ($\lambda = 799.7$ nm), which is close to the peak of the ASE spectrum at $\lambda = 791$ nm ($\lambda = 803$ nm). Above the lasing threshold, the emission rate through biexciton or single-exciton recombination increases considerably, benefiting the stimulated radiation over spontaneous recombination⁵².

The lasing feature of the MAPbI₃ VCSEL is investigated by collecting the light emission under a backscattering configuration. The light emission spectra of the tetragonal VCSEL under different pumping fluences are measured at 130 K and shown in the left column of Fig. 3(a). A weak broad radiation spectrum is observed for $F_{\text{pump}} < 48$ μJ cm⁻², which is dominated by the PL spectrum³². At a larger fluence of $F_{\text{pump}} = 55.7$ μJ cm⁻², a single narrow lasing emission peak appears at 790.6 nm. Figure 3(a) shows the light-light (L-L) curve and FWHMs of the PL spectra of the 790.6 nm peak under different pumping fluences. The threshold energy density of lasing appears around 48 μJ cm⁻², where the FWHM shrinks sharply from 18 nm to 0.7 nm. When the MAPbI₃ layer undergoes a phase change from tetragonal to orthorhombic, the lasing wavelength changes from 790.6 nm to 799.7 nm, as shown in the left column of Fig. 3(b). In Fig. S7, we have measured the emission spectra of VCSEL at the temperatures of 130K, 140K, 150 K and 160 K, respectively. The tuning rate was the ratio of the shift of wavelength with respect to the change of temperature, which is approximately 0.30 nm K⁻¹ rate.

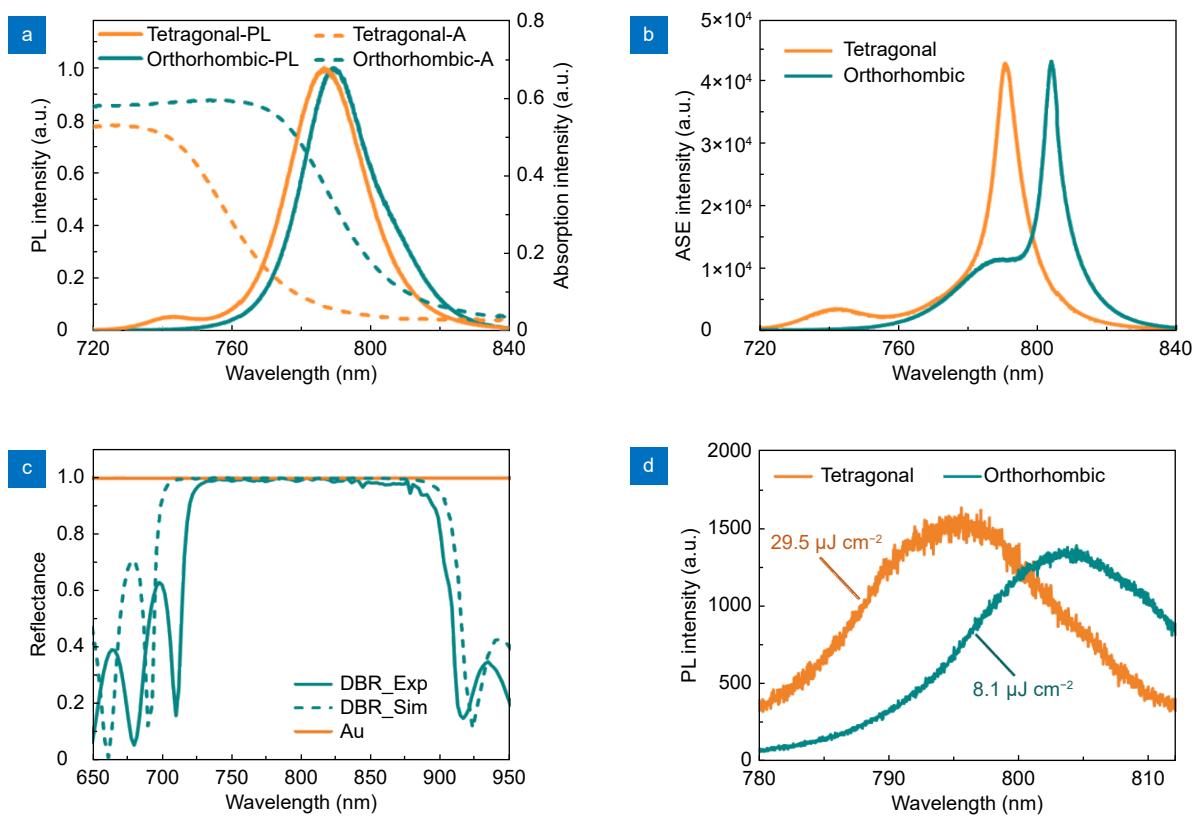


Fig. 2 | (a) The absorbance and PL spectra of MAPbI₃ nanocrystalline film with tetragonal (130 K, orange line) and orthorhombic (160 K, green line) states, respectively. (b) The ASE spectra of MAPbI₃ phase change perovskite with the structural states of tetragonal (130 K, orange line) and orthorhombic (160 K, green line), respectively. (c) Reflectance spectra of top Au flake (orange line) and bottom DBR (green line), the green dashed line is the simulation of the bottom DBR reflectance spectra. (d) The measured PL spectra of the MAPbI₃ based microcavity with the different states of tetragonal (29.5 μJ cm⁻²) and orthorhombic (8.1 μJ cm⁻²).

Meanwhile, the state transition redshifts the absorbance edge of MAPbI₃, leading to a better spectral overlap between the gain and lasing mode of the vertical cavity. Consequently, the lasing threshold decreases to ~23.5 μJ cm⁻² at 160 K for the orthorhombic VCSEL (the right column of Fig. 3(b)). In supplementary Fig. S8, the laser characteristics of MAPbI₃ VCSEL were investigated at 135 K, 140 K, and 150 K by analyzing light emission in the backscattering configuration. The light emission spectra of the VCSEL under various pump fluences were measured at 135 K, as illustrated in the upper row of Fig. S8(a). At pump fluences below 42 μJ cm⁻², a weak, broad emission spectrum was observed. When the pump fluence increased to 42.8 μJ cm⁻², a single, narrow lasing emission peak emerged at approximately 792 nm. Similar laser performance was observed at 140 K and 150 K. At 140 K, the laser emission peak was centered around 793.5 nm, with a lasing threshold of approximately 24.9 μJ cm⁻². At 150 K, the lasing threshold decreased to approximately 22.2 μJ cm⁻², and the central wavelength of

the laser emission peak shifted to about 796.5 nm.

To examine the temperature dependence of the lasing threshold, L-L curves of the VCSEL were measured across temperatures ranging from 130 K to 160 K, with the results presented in Fig. 4(a). The laser characteristics of the MAPbI₃ VCSEL at 135 K, 140 K, and 150 K are detailed in supplementary Fig. S8. Notably, the lasing threshold exhibits an unusual trend, first decreasing and then slightly increasing (Fig. 4(b)), deviating from the typically observed monotonic increase in lasing threshold with rising temperature⁵⁵. The reduction in the lasing threshold between 160 K and 150 K is attributed to a decrease in Auger recombination losses and an increase in the bimolecular recombination constant and radiative recombination rate as the temperature decreases. These factors facilitate population inversion and laser emission at lower pump energy densities⁵⁶. Interestingly, the Auger recombination rate of MAPbI₃ is highly phase-dependent, significantly decreasing in the orthorhombic phase but increasing several-fold in the tetragonal

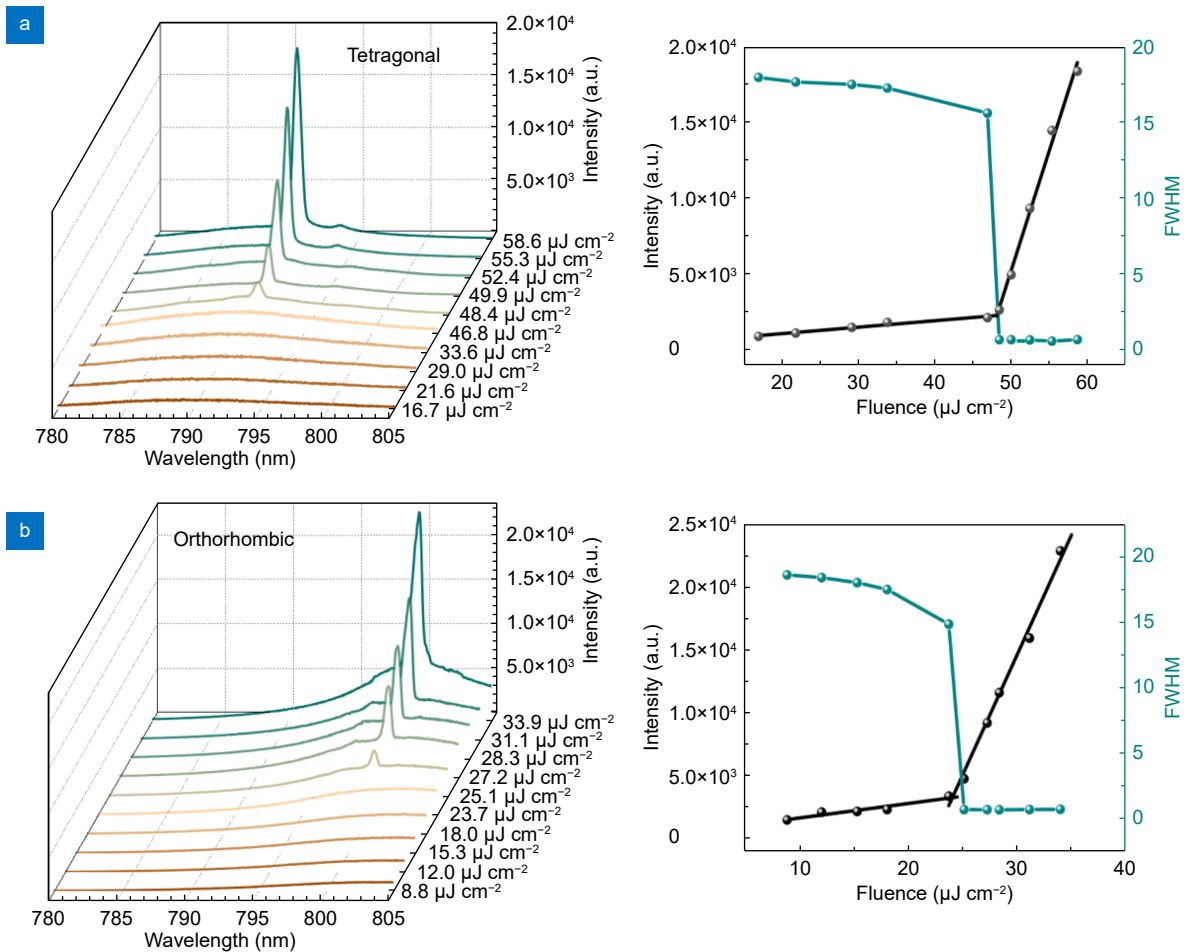


Fig. 3 | Laser performance of the VCSEL microlaser at different perovskite phase states. (a) Performance of the VCSEL microlasers based on the tetragonal MAPbI₃: 130 K radiation spectra of the VCSEL against pump fluence (left column); light-light curve of the tetragonal laser at 130 K (right column). (b) Performance of the VCSEL with the orthorhombic MAPbI₃: room-temperature radiation spectra of the VCSEL against pump fluence (left column); light-light curve of the orthorhombic laser at 160 K (right column).

phase⁵⁷. The sudden increase in the lasing threshold at 130 K and 135 K is ascribed to a phase transition in the MAPbI₃ active layer from orthorhombic to tetragonal as the temperature decreases, causing a sharp rise in Auger recombination losses. Within the temperature range of 140 K to 150 K, the perovskite active layer exists in a mixed phase state, with the lasing threshold influenced by both the temperature and the ongoing phase transition of the perovskite.

We further measure the lifetime of VCSEL devices under continuous pulse excitation (405 nm, 130 fs, 8 kHz) at both the tetragonal and orthorhombic states. We optically pump the devices to $1.1 F_{th}$ (F_{th} represented the threshold pump fluence) under ambient conditions and record the integrated radiation intensities against time. An 80% lifetime (T_{80}) is defined as the time when the output intensity is reduced to 80% of the initial power.

This tunable perovskite VCSEL could be investigating the properties of superconducting materials, where the superconducting phenomenon typically occurs under low-temperature conditions, this laser could provide a stable, wavelength-tunable light source. Such a light source would be ideal for probing the optical response characteristics of superconducting materials across different superconducting states, such as changes in reflectivity and absorptivity. This capability would facilitate a deeper understanding of the underlying superconducting mechanisms and the material properties. As can be seen in Fig. 4(c), the laser intensity decreases relatively slowly, maintaining 80% of initial level after ~50 mins (2.4×10^7 pumping pulses). For the orthorhombic state, the VCSEL under the fs pumping pulses possesses even better stability ($T_{80} > 2$ h/ 5.76×10^7 pumping pulses). It was found that this pulse count is comparable to values

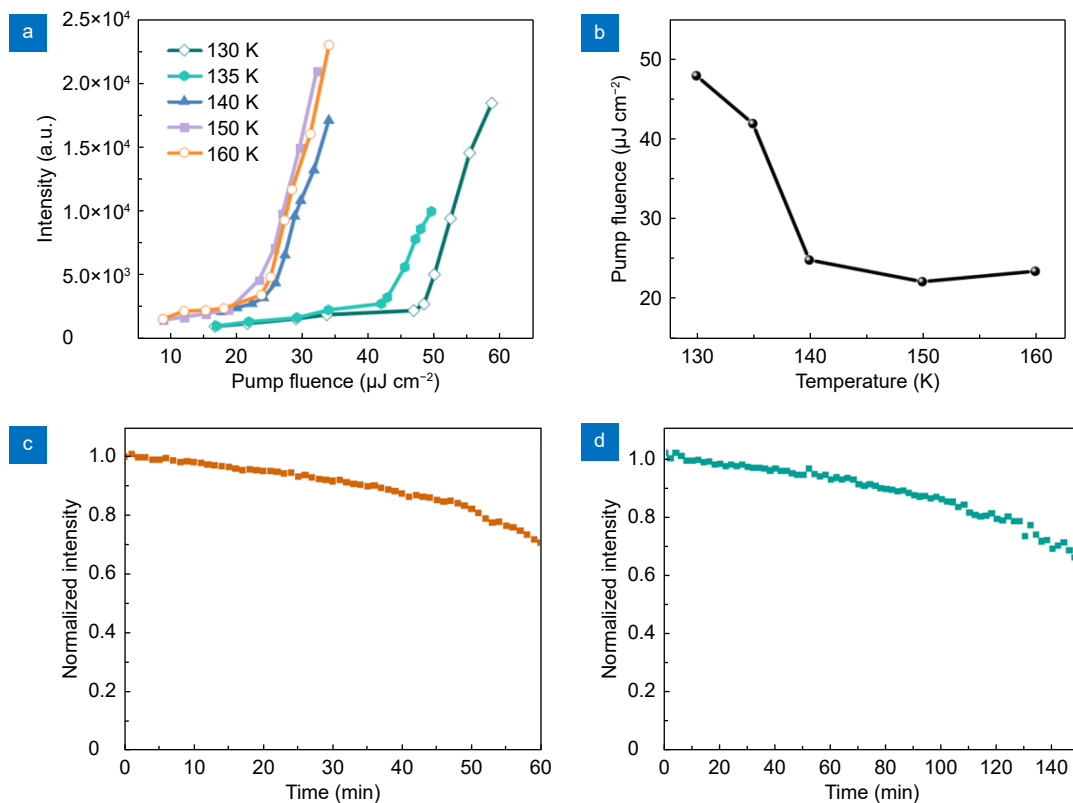


Fig. 4 | (a) The L - L curve for the MAPbI₃ VCSEL by increasing the temperature from 130 K to 160 K. (b) Lasing threshold pumping fluence versus temperature for the device. Stability characterizations of the VCSEL under fs pulsed excitation with pumping fluence at $1.1 F_{th}$ for both (c) tetragonal and (d) orthorhombic states, respectively.

reported in existing studies on perovskite lasers excited by pulses of the same category^{58–61}. We also demonstrate that the device exhibits good operational stability during the transition from tetragonal to orthorhombic state, as shown in Fig. 4(d). Recent studies have explored MAPbI₃-based perovskite lasers employing various structures, including symmetric waveguides⁶², WGM⁶³, DFB⁶⁴, PC⁶⁵, and vertical cavities⁶⁶. However, these designs exhibit notable limitations. For instance, symmetric waveguide lasers display a relatively broad FWHM of approximately 3 nm, while DFB and PC perovskite lasers require significantly high lasing thresholds ($\sim 200 \mu\text{J cm}^{-2}$). Additionally, none of these approaches offer a tunable operating wavelength. In contrast, our proposed structure demonstrates a distinct advantage with a tunable lasing wavelength range of 790.6 nm to 799.7 nm, a considerably narrower FWHM of 0.7 nm, and a significantly lower lasing threshold of approximately $22 \mu\text{J cm}^{-2}$, outperforming previously reported designs.

Conclusions

We have demonstrated a tunable perovskite VCSEL by

integrating MAPbI₃ thin film with a Fabry-Perot cavity, composed of a top DBR and a bottom Au mirror. Our approach combines the NCs with judiciously designed resonance cavity. This was achieved via the optimization of the MAPbI₃ layer thickness and the DBR reflector geometry, which enabled a single-mode lasing emission with both high Q factors and low threshold lasing intensities for both tetragonal and orthorhombic states. Importantly, large tunability is achieved by altering the state of MAPbI₃ perovskite, resulting in a shift of lasing wavelength from 790.6 nm to 799.7 nm. Moreover, the utilization of MAPbI₃ film ensured high stability of VCSEL, with the device maintaining its performance over hours of operation at femtosecond pulsed pumping under ambient conditions. Our work may offer new opportunities for space and wavelength division multiplexing applications in optics communications, dense neuromorphic devices and optical readout detectors. Moreover, we anticipate that the realization of highly efficient and stable electrically injected perovskite lasers would pave the way for the development of miniaturized, low-power laser sources. This advancement would lay a solid foundation

for their practical implementation in various applications and open up a promising avenue for future research.

Experimental section

Growth of the MAPbI₃ film on the quartz

We have made ultrathin MAPbI₃ film from 1.2 M predecessor solution of PbI₂ (99.99%, TCI) and CH₃NH₃I (Dyesol) (molar ratio 1:1) in anhydrous dimethylformamide (DMF, Sigma-Aldrich). The prepared solution was magnetically stirred overnight under room temperature in a glovebox filled with N₂, then filtered by a polyvinylidene fluoride (PVDF) syringe filter (0.45 μm) and left on the hot plate under 373 K for ~1 hour before spin-coating. Before the deposition of perovskite, quartz substrates were cleaned using the solution: Hellmanex II (Hellma Analytics, 2 mL) in deionized (DI) water (200 mL) under a temperature of 353 K for 10 min. Afterwards, the substrate was washed with DI water and dried with the nitrogen flow and cleaning treatment of oxygen plasma. We have spin-coated the perovskite precursor solution onto the quartz substrates at a speed of 5100 rpm for 30 s using antisolvent engineering method. It can be seen from Fig. S6(b) that the thickness of the perovskite film is about 300 nm when the spin coating speed is 5100 rpm. We drop-casted the toluene on the substrates with a spin-coating duration of 5 s. The films were thermally annealed at 373 K for 15 min.

Fabrication of MAPbI₃ based VCSEL

Firstly, the DBR mirror with ~99.8% reflectance for 795 nm were fabricated on a quartz glass substrate using Magnetron Sputter Deposition system (AJA Orion5). The DBR (12 pairs of Ta₂O₅/SiO₂ alternating layers) is directly sputtered onto quartz. Secondly, we have cleaned out the DBR mirror with acetone, 2-propanol, and deionized water under sonication for 15 min. Thirdly, the cleaned DBR mirrors were processed with oxygen plasma for 10 min before a spin-coating process. After that, MAPbI₃ film was grown on the DBR substrate using the method above. And after perovskite film deposition, a high-quality Au film (100 nm) was deposited on the MAPbI₃ films to act as the back reflector by magnetron sputtering.

Characterization of perovskite MAPbI₃

The surface morphology of MAPbI₃ films was measured by optical microscope (Olympus BX53M). We have mea-

sured the surface roughness of MAPbI₃ film grown on the quartz substrate by the atomic force microscope (AFM, Park NX10). High-resolution SEM was performed using a Field emission scanning electron microscope (JSM-7900F) at 5 kV. We have investigated the temperature-dependent XRD spectra of the MAPbI₃ film. We have employed a Bruker F8 Focus power XRD with monochromatized Cu Kα radiation ($\lambda = 1.5418 \text{ \AA}$) to record powder XRD patterns of MAPbI₃ film residing on the quartz glass substrate. We measured UV-visible absorbance spectra of the MAPbI₃ using SHIMADZU UV-3600Plus spectrophotometer. Both the steady-state photoluminescent emission spectrum and the amplified spontaneous emission (ASE) spectrum were measured using a home-built micro-photoluminescence (μ -PL) system. Light from a 405 nm laser was focused onto the MAPbI₃ film using a 4 ×, 0.1 NA objective lens. The PL signal was collected by the same objective lens and directed to a spectrometer integrated with a CCD detector cooled by liquid nitrogen (Princeton HRS-500) with a maximum grating density of 1800 g mm⁻¹ grating. For the measurement of photoluminescence spectrum, a 405 nm continuous wavelength laser (PicoQuant) was used as the pumping source. For the ASE spectrum, a 405 nm pulsed laser (pulse width: 130 fs, repetition rate: 80 kHz) was used as the pumping source. To minimize the influence of ambient light, the entire experimental system was covered with a black cloth.

Characterization of laser devices

The lasing characterizations were carried out on a home-built micro-photoluminescence (μ -PL) system at low temperature in a vacuumed atmosphere. A femtosecond pulsed laser (wavelength: 405 nm, pulse width: 130 fs, repetition rate: 8 kHz) was used as the excitation source, which was focused by a microscopy objective (50 ×), and this was used for the excitation of the samples. The excitation laser spot was around 30 μm in diameter. The resulting signal was collected by the same objective lens and directed to a spectrometer with a grating density of 1200 g mm⁻¹. Low-temperature measurement was performed in a cryostat (Montana Instruments S50). The entire experimental system was still covered with a black cloth.

Simulations

The simulated reflectance spectra in Fig. 2(c) were performed by the Ansys Optics software relied on the 2D

Finite-Different-Time-Domain (FDTD) method. The periodic boundary condition conditions were used in the x - y plane and the perfectly matched layer (PML) condition was defined along vertical direction (z -axis). A plane wave source located near the perovskite layer was used to excite the system, and the reflectance was numerically achieved via a power monitor located in front of the device. A uniform FDTD square mesh (5 nm \times 5 nm \times 5 nm) was employed to diminish the numerical error during the FDTD calculation. Our numerical models defined the Au with the losses using Palik permittivity data. The permittivity of the perovskite MAPbI₃ film under both structural phases of tetragonal and orthorhombic were defined from the VASE experimentally measured ones in Fig. S1.

References

- Huang C, Zhang C, Xiao SM et al. Ultrafast control of vortex microlasers. *Science* **367**, 1018–1021 (2020).
- Zhu HM, Fu YP, Meng F et al. Lead halide perovskite nanowire lasers with low lasing thresholds and high quality factors. *Nat Mater* **14**, 636–642 (2015).
- Sun WZ, Liu YL, Qu GY et al. Lead halide perovskite vortex microlasers. *Nat Commun* **11**, 4862 (2020).
- Adamo G, Swaha Krishnamoorthy HN, Cortecchia D et al. Meta-material enhancement of metal-halide perovskite luminescence. *Nano Lett* **20**, 7906–7911 (2020).
- Karlsson M, Yi ZY, Reichert S et al. Mixed halide perovskites for spectrally stable and high-efficiency blue light-emitting diodes. *Nat Commun* **12**, 361 (2021).
- Makarov S, Furasova A, Tiguntseva E et al. Halide - perovskite resonant nanophotonics. *Adv Opt Mater* **7**, 1800784 (2019).
- Jeong J, Kim M, Seo J et al. Pseudo-halide anion engineering for α -FAPbI₃ perovskite solar cells. *Nature* **592**, 381–385 (2021).
- Shen XY, Gallant BM, Holzhey P et al. Chloride - based additive engineering for efficient and stable wide - bandgap perovskite solar cells. *Adv Mater* **35**, 2211742 (2023).
- Li ZG, Cao Y, Feng JS et al. Stable and high - efficiency perovskite solar cells using effective additive ytterbium fluoride. *Small* **19**, 2303017 (2023).
- Swarnkar A, Marshall AR, Sanehira EM et al. Quantum dot-induced phase stabilization of α -CsPbI₃ perovskite for high-efficiency photovoltaics. *Science* **354**, 92–95 (2016).
- Chiba T, Hayashi Y, Ebe H et al. Anion-exchange red perovskite quantum dots with ammonium iodine salts for highly efficient light-emitting devices. *Nat Photonics* **12**, 681–687 (2018).
- Hao MM, Bai Y, Zeiske S et al. Ligand-assisted cation-exchange engineering for high-efficiency colloidal Cs_{1-x}FA_xPbI₃ quantum dot solar cells with reduced phase segregation. *Nat Energy* **5**, 79–88 (2020).
- Deschler F, Price M, Pathak S et al. High photoluminescence efficiency and optically pumped lasing in solution-processed mixed halide perovskite semiconductors. *J Phys Chem Lett* **5**, 1421–1426 (2014).
- Pina JM, Parmar DH, Bappi G et al. Deep - blue perovskite single - mode lasing through efficient vapor - assisted chlorination. *Adv Mater* **33**, 2006697 (2021).
- Chen ST, Roh K, Lee J et al. A photonic crystal laser from solution based organo-lead iodide perovskite thin films. *ACS Nano* **10**, 3959–3967 (2016).
- Wu XX, Zhang S, Song JP et al. Exciton polariton condensation from bound states in the continuum at room temperature. *Nat Commun* **15**, 3345 (2024).
- Sutherland BR, Hoogland S, Adachi MM et al. Conformal organohalide perovskites enable lasing on spherical resonators. *ACS Nano* **8**, 10947–10952 (2014).
- Zhang Q, Su R, Liu XF et al. High - quality whispering - gallery - mode lasing from cesium lead halide perovskite nanoplatelets. *Adv Funct Mater* **26**, 6238–6245 (2016).
- Song JP, Shang QY, Deng XY et al. Continuous - wave pumped perovskite lasers with device area below 1 μm^2 . *Adv Mater* **35**, 2302170 (2023).
- Qin CJ, Sandanayaka ASD, Zhao CY et al. Stable room-temperature continuous-wave lasing in quasi-2D perovskite films. *Nature* **585**, 53–57 (2020).
- Harwell JR, Whitworth GL, Turnbull GA et al. Green perovskite distributed feedback lasers. *Sci Rep* **7**, 11727 (2017).
- Kurahashi N, Runkel M, Kreusel C et al. Distributed feedback lasing in thermally imprinted phase - stabilized CsPbI₃ thin films. *Adv Funct Mater* **34**, 2405976 (2024).
- Allegro I, Bonal V, Mamleyev ER et al. Distributed feedback lasers by thermal nanoimprint of perovskites using gelatin gratings. *ACS Appl Mater Interfaces* **15**, 8436–8445 (2023).
- Wang Q, Rogers ETF, Gholipour B et al. Optically reconfigurable metasurfaces and photonic devices based on phase change materials. *Nat Photonics* **10**, 60–65 (2016).
- Zhang SJ, Chen XY, Liu K et al. Nonvolatile reconfigurable terahertz wave modulator. *PhotonIX* **3**, 7 (2022).
- Mao LB, Li Y, Li GX et al. Reversible switching of electromagnetically induced transparency in phase change metasurfaces. *Adv Photonics* **2**, 056004 (2020).
- Cao T, Lian M, Chen XY et al. Multi-cycle reconfigurable THz extraordinary optical transmission using chalcogenide metamaterials. *Opto-Electron Sci* **1**, 210010 (2022).
- Liu K, Lin ZY, Han B et al. Non-volatile dynamically switchable color display via chalcogenide stepwise cavity resonators. *Opto-Electron Adv* **7**, 230033 (2024).
- Zhu ZH, Evans PG, Haglund RF Jr et al. Dynamically reconfigurable metadvice employing nanostructured phase-change materials. *Nano Lett* **17**, 4881–4885 (2017).
- Yuan R, Tiw PJ, Cai L et al. A neuromorphic physiological signal processing system based on VO₂ memristor for next-generation human-machine interface. *Nat Commun* **14**, 3695 (2023).
- Shaltout AM, Shalaev VM, Brongersma ML. Spatiotemporal light control with active metasurfaces. *Science* **364**, eaat3100 (2019).
- Zhang HB, Hu YZ, Wen W et al. Room-temperature continuous-wave vertical-cavity surface-emitting lasers based on 2D layered organic-inorganic hybrid perovskites. *APL Mater* **9**,

- 071106 (2021).
33. Zhan Y, Li C, Che ZG et al. Light management using photonic structures towards high-index perovskite optoelectronics: fundamentals, designing, and applications. *Energy Environ Sci* **16**, 4135–4163 (2023).
 34. Chin XY, Cortecchia D, Yin J et al. Lead iodide perovskite light-emitting field-effect transistor. *Nat Commun* **6**, 7383 (2015).
 35. Xing GC, Mathews N, Lim SS et al. Low-temperature solution-processed wavelength-tunable perovskites for lasing. *Nat Mater* **13**, 476–480 (2014).
 36. Makarov SV, Milichko V, Ushakova EV et al. Multifold emission enhancement in nanoimprinted hybrid perovskite metasurfaces. *ACS Photonics* **4**, 728–735 (2017).
 37. Caligiuri V, Siprova S, Godbert N et al. Enhanced spontaneous emission through high - k modes in CsPbBr₃ perovskite hyperbolic metamaterials. *Laser Photonics Rev* **18**, 2301156 (2024).
 38. Gholipour B, Adamo G, Cortecchia D et al. Organometallic perovskite metasurfaces. *Adv Mater* **29**, 1604268 (2017).
 39. Gao YS, Huang C, Hao CL et al. Lead halide perovskite nanostructures for dynamic color display. *ACS Nano* **12**, 8847–8854 (2018).
 40. Fan YB, Wang YH, Zhang N et al. Resonance-enhanced three-photon luminescence via lead halide perovskite metasurfaces for optical encoding. *Nat Commun* **10**, 2085 (2019).
 41. Xing D, Lin CC, Ho YL et al. Ligand engineering and recrystallization of perovskite quantum - dot thin film for low - threshold plasmonic lattice laser. *Small* **18**, 2204070 (2022).
 42. Huang SH, Shen ZX, Liao Y et al. Water - resistant subwavelength perovskite lasing from transparent silica - based nanocavity. *Adv Mater* **35**, 2306102 (2023).
 43. Liu ZZ, Hu MC, Du J et al. Subwavelength-polarized quasi-two-dimensional perovskite single-mode nanolaser. *ACS Nano* **15**, 6900–6908 (2021).
 44. Ma ZW, Liu Z, Lu SY et al. Pressure-induced emission of cesium lead halide perovskite nanocrystals. *Nat Commun* **9**, 4506 (2018).
 45. Wang YT, Quintana X, Kim J et al. Phase segregation in inorganic mixed-halide perovskites: from phenomena to mechanisms. *Photonics Res* **8**, A56–A71 (2020).
 46. Sun B, Liu XF, Li XY et al. Reversible thermochromism and strong ferromagnetism in two - dimensional hybrid perovskites. *Angew Chem Int Ed* **59**, 203–208 (2020).
 47. Jiang YJ, Soufiani AM, Gentle A et al. Temperature dependent optical properties of CH₃NH₃PbI₃ perovskite by spectroscopic ellipsometry. *Appl Phys Lett* **108**, 061905 (2016).
 48. Blancon JC, Even J, Stoumpos CC et al. Semiconductor physics of organic–inorganic 2D halide perovskites. *Nat Nanotechnol* **15**, 969–985 (2020).
 49. Zhang LX, Mei LY, Wang KY et al. Advances in the application of perovskite materials. *Nano-Micro Lett* **15**, 177 (2023).
 50. Yonemura M. Wavelength-change characteristics of semiconductor lasers and their application to holographic contouring. *Opt Lett* **10**, 1–3 (1985).
 51. Kong WG, Ye ZY, Qi Z et al. Characterization of an abnormal photoluminescence behavior upon crystal-phase transition of perovskite CH₃NH₃PbI₃. *Phys Chem Chem Phys* **17**, 16405–16411 (2015).
 52. Yakunin S, Protesescu L, Krieg F et al. Low-threshold amplified spontaneous emission and lasing from colloidal nanocrystals of caesium lead halide perovskites. *Nat Commun* **6**, 8056 (2015).
 53. Dang C, Lee J, Breen C et al. Red, green and blue lasing enabled by single-exciton gain in colloidal quantum dot films. *Nat Nanotechnol* **7**, 335–339 (2012).
 54. Li XH, Liu WW, Song YL et al. Two-photon-pumped high-quality, single-mode vertical cavity lasing based on perovskite monocrystalline films. *Nano Energy* **68**, 104334 (2020).
 55. Cadelano M, Sarritzu V, Sestu N et al. Can trihalide lead perovskites support continuous wave lasing. *Adv Opt Mater* **3**, 1557–1564 (2015).
 56. Jia YF, Kerner RA, Grede AJ et al. Diode-pumped organo-lead halide perovskite lasing in a metal-clad distributed feedback resonator. *Nano Lett* **16**, 4624–4629 (2016).
 57. Milot RL, Eperon GE, Snaith HJ et al. Temperature - dependent charge - carrier dynamics in CH₃NH₃PbI₃ perovskite thin films. *Adv Funct Mater* **25**, 6218–6227 (2015).
 58. Whitworth GL, Harwell JR, Miller DN et al. Nanoimprinted distributed feedback lasers of solution processed hybrid perovskites. *Opt Express* **24**, 23677–23684 (2016).
 59. Fu YP, Zhu HM, Schrader AW et al. Nanowire lasers of formamidinium lead halide perovskites and their stabilized alloys with improved stability. *Nano Lett* **16**, 1000–1008 (2016).
 60. Shi ZF, Zhang F, Yan JJ et al. Robust frequency-upconversion lasing operated at 400 K from inorganic perovskites microcavity. *Nano Res* **15**, 492–501 (2022).
 61. Cao XH, Xing SY, Lai RC et al. Low - threshold, external - cavity - free flexible perovskite lasers. *Adv Funct Mater* **33**, 2211841 (2023).
 62. Zeng X, Liu ZZ, Du HJ et al. Achieving low threshold and high optical gain amplified spontaneous emission in MAPbI₃ perovskite films via symmetric waveguide effect. *Adv Opt Mater* **10**, 2201328 (2022).
 63. Li GH, Tao JX, Hou Z et al. Room - temperature single - mode plasmonic perovskite nanolasers with sub - picosecond pulses. *Adv Funct Mater* **34**, 2405559 (2024).
 64. Li ZT, Moon J, Gharajeh A et al. Room-temperature continuous-wave operation of organometal halide perovskite lasers. *ACS Nano* **12**, 10968–10976 (2018).
 65. Cha H, Bae S, Lee M et al. Two-dimensional photonic crystal bandedge laser with hybrid perovskite thin film for optical gain. *Appl Phys Lett* **108**, 181104 (2016).
 66. Chen ST, Zhang C, Lee J et al. High - Q, low - threshold monolithic perovskite thin - film vertical - cavity lasers. *Adv Mater* **29**, 1604781 (2017).

Acknowledgements

This work was financially supported by the National Key Research and Development Program of China (2020YFA0714504, 2019YFA0709100 to T.C.), the program of the National Natural Science Foundation of China (No. 62105054 to T.C.), the New Cornerstone Science Foundation (AoE/P-502/20 to S.Z.), the Research Grants Council of Hong Kong (17315522 to S.Z.).

Author contributions

Rongzi Wang, Ying Su and Tun Cao contributed equally to this work. The manuscript was written through contributions of all authors. All authors have given approval to the final version of the manuscript.

Supplementary information

Supplementary information for this paper is available at <https://doi.org/10.29026/oea.2025.240220>

Competing interests

The authors declare no competing financial interests.



Scan for Article PDF